

RAIDER: Rapid, anatomy-independent, deep learning-based PDFF and R_2^* estimation using magnitude-only signals

Timothy JP Bray^{1,2,3}  | Giulio V Minore³  | Alan Bainbridge^{1,4}  | Louis Dwyer-Hemmings^{1,2,3}
| Stuart A Taylor^{1,2}  | Margaret A Hall-Craggs^{1,2}  | Hui Zhang³ 

¹Centre for Medical Imaging, University College London, London, United Kingdom

²Department of Imaging, University College London Hospital, London, United Kingdom

³Department of Computer Science and Centre for Medical Image Computing, University College London, London, United Kingdom

⁴Department of Medical Physics, University College London Hospital, London, United Kingdom

Correspondence

Timothy J.P. Bray, Centre for Medical Imaging, University College London, 2nd Floor Charles Bell House, 43-45 Foley Street, W1W 7TS. Email: t.bray@ucl.ac.uk

Funding Information

This work was supported by The National Institute for Health Research (NIHR) Biomedical Research Centre (BRC); grant BRC1121/HEI/TB/110410. Timothy Bray receives personal support from the National Institute for Health Research Biomedical Research Centre. Giulio Minore is supported by the EPSRC-funded UCL Centre for Doctoral Training in Intelligent, Integrated Imaging in Healthcare (i4health) (EP/S021930/1) and the NIHR BRC at University College London Hospitals.

Purpose: There has been substantial recent interest in magnitude-based fitting methods for estimating proton density fat fraction (PDFF) and R_2^* from chemical shift-encoded MRI data, since these methods can still be used when complex-based methods fail or when phase data are inaccessible or unreliable, and may also be used as a final processing step with complex-based methods. However, conventional fitting techniques are computationally expensive. Deep learning (DL)-based methods promise to accelerate parameter estimation, but previous attempts have used convolutional neural networks (CNNs), which are limited by training requirements and poor generalizability ('anatomy-dependence'). To address these limitations, we propose RAIDER, a voxelwise method for rapid, anatomy-independent deep learning-based PDFF and R_2^* estimation using multi-echo magnitude-data.

Theory and Methods: RAIDER uses two multilayer perceptrons, each trained separately with simulated single-voxel multi-echo magnitude signals, to estimate PDFF and R_2^* . The use of two networks, each with restricted training distribution, solves the problem of degeneracy during training. During inference, the solution from one of the two networks is chosen based on likelihood. Performance and speed are investigated in a series of simulation experiments, in phantoms and *in vivo*.

Results: RAIDER is 285-1450 times faster than conventional magnitude fitting, taking 1.4-2.3s per slice rather than 8-56minutes, and offers performance similar to conventional fitting. It produces accurate PDFF measurements in phantoms and *in vivo* images with different anatomies, despite having been trained only on simulation data.

Conclusion: RAIDER can substantially accelerate magnitude-based PDFF and R_2^* estimation, whilst avoiding intrinsic limitations of CNN-based methods.

KEYWORDS:

deep learning, computer-assisting image processing, magnetic resonance imaging, radiology

Chemical shift-encoded MRI (CSE-MRI) is a reliable, fast method for quantifying proton density fat fraction (PDFF) in a wide variety of organs and disease states^{1,2,3,4,5,6}. PDFF measurements are now established for the measurement of steatosis in liver⁵, and are also increasingly used for other organs including pancreas^{7,8}, muscle⁹ and bone marrow^{10,11}. CSE-MRI most commonly utilises multi-echo gradient echo acquisitions, meaning that R_2^* measurements can be extracted from the same acquisition, providing additional quantitative information on iron or calcium. PDFF and R_2^* measurements estimated using gradient echo acquisitions therefore offer flexible biomarkers informing on a wide variety of pathological processes. The speed of the underpinning acquisitions means that these biomarkers can also be acquired in the context of whole body MRI (WB-MRI), which is becoming an important tool for cancer staging^{12,13,14}, amongst other applications such as the assessment of inflammatory arthritis¹⁵.

From a signal processing perspective, the central challenge of CSE-MRI is to disentangle or separate the signals arising from water and fat. This is challenging because the signal arising from water-dominant and fat-dominant tissues is very similar, giving rise to the so-called ‘fat-water ambiguity’ problem. The prevailing approach to solving this problem has been to use the phase of the complex signal in order to separate water and fat: with complex signal-based methods, water-dominant and fat-dominant tissues can be distinguished on the basis of their phase, so long as the contribution to the phase from main magnetic field B_0 can be estimated accurately and therefore separated from the phase arising due to chemical shift^{1,2,3,4,5}. Despite the progress that has been achieved by these complex-based methods^{1,2,3,4,5}, fat-water swaps still occur and can mimic or hide important abnormalities¹⁶, meaning that avoiding such swaps remains a research focus, both for standard gradient echo CSE-MRI¹⁷ and to enable the estimation of fat-corrected qMRI parameters¹⁸. Additionally, in some situations (such as in multi-centre studies or less well-resourced clinical settings), complex data (and/or expensive vendor-supplied software packages for PDFF estimation) may not be available, constituting a substantial barrier to the use of CSE-MRI and a potential source of geographic inequality. Finally, in emerging fields such as imaging near metal¹⁹ and small bowel MRI²⁰, fat suppression methods need to deal with large B_0 variations, where existing fat suppression methods commonly fail.

As a result of these limitations, a different class of methods using only the magnitude of the signal (i.e. where the signal phase is discarded) for parameter estimation have been developed. These magnitude-based methods avoid the difficulty in estimating B_0 , but require a further source of information to resolve fat-water ambiguity. Recently, the MAGO and

MAGORINO methods were developed to resolve this ambiguity, showing that fat- and water-dominant tissues could be distinguished on the basis of subtle differences in the oscillations of the magnitude signal over multiple echoes^{21,22}. In addition to being usable in situations where complex data and/or expensive vendor-supplied software packages are not available, these methods also avoid phase errors which can induce bias when fitting with complex data, meaning that they may be more accurate and robust than complex signal-based techniques in a real-world setting. Related to these advantages, the MAGO technique (not developed by these authors) has achieved regulatory clearance within the Liver-Multiscan package (Perspectum, Oxford) and is increasingly being used in clinical trials^{23,24,25}. Magnitude-based fitting is also commonly used as a final processing step even in complex fitting pipelines²⁶, and is the central fitting method used in the Siemens qDixon package²⁷. There has also been interest in using magnitude-fitting as a first processing step in order to improve estimation of B_0 inhomogeneity, with a view to performing quantitative susceptibility mapping (QSM)¹⁸.

Although these magnitude-based methods have a number of advantages in terms of accessibility and practicality, and promise to widen access to the use of these methods, they do carry a substantial computational cost, due to the iterative nature of the algorithms as well as the need to perform fitting with nonlinear least squares several times - with different start points - in order to ensure that the correct likelihood maximum / error minimum is found^{21,22}. This increases the time, human resource and funding required to use these techniques, limiting their use in research settings and in clinical practice.

A promising approach to reducing this computational cost is to use deep learning for parameter estimation: this has the advantage that computational cost is front-loaded: training can be performed in advance, before images are acquired, and the computational resources needed to actually process those images are typically much less than with conventional fitting^{28,29,30}. However, so far, for the purposes of fat-water separation, most authors have used convolutional neural networks, taking signals from the whole image as input, to separate fat and water^{31,32,33,34}. These methods exploit the spatial relationships in the image as well as the information contained within individual voxels in the echo dimension. A disadvantage of the CNN-based approach is that training is typically performed on real images from a specific anatomical region, meaning that large, expensive datasets are typically required to achieve satisfactory real-world performance. Furthermore, methods trained in this way are very unlikely to be fully generalizable to other regions of the body or to pathological cases. CNN-based methods are also highly vulnerable to differences in acquisition parameters such as image matrix, and training networks using this approach is typically extremely slow, with training taking many hours or even days^{31,32,33,34}. In contrast, voxel-independent methods^{28,29,30} have the advantage that there is

no inherent dependence on anatomy, pathology or acquisition geometry introduced during training, making them potentially much more generalizable across anatomies, scanners and imaging protocols. These methods can also be trained in simulation, substantially reducing cost and removing a barrier to their use. However, there is no existing voxel-independent (i.e. non-CNN) deep learning-based method for magnitude fitting.

To address this problem, here we investigate the use of multilayer perceptrons (MLPs) for PDFF and R_2^* estimation from multi-echo magnitude signals. We first identify a crucial problem with a ‘naive’ single MLP implementation, related to model degeneracy: the network performs poorly because multiple combinations of parameter values can produce very similar signals. To solve this degeneracy problem, we propose a novel method whereby two MLPs, each trained separately with a restricted training distribution, are used to avoid degeneracy and thus estimate these parameters. The new method is referred to as RAIDER: rapid, anatomy-independent deep learning-based CSE-MRI.

2 | THEORY

2.1 | Tissue and noise models

A full description of the tissue and noise models used in this work is given in²²; the key tissue and noise models are briefly summarised here.

With a gradient echo-based CSE-MRI acquisition, the noise-free complex signal S acquired at echo time t can be modelled as:

$$S(t|S_0, PDFF, R_2^*, f_B) = S_0 \left((1 - PDFF) + PDFF \sum_{m=1}^M r_m e^{i2\pi f_{F,m} t} \right) e^{i2\pi f_B t} e^{-tR_2^*} \quad (1)$$

where S_0 and $PDFF$ are the theoretical signal intensity at $t=0$ and proton density fat fraction respectively, $f_{F,m}$ is the frequency of each spectral fat component, r_m is the relative amplitude of each spectral fat component, M is the total number of spectral fat components, f_B is the frequency offset due to B_0 inhomogeneity and $R_2^* = 1/T_2^*$ is an unknown relaxation constant. It is conventional to assume that the relative amplitudes and frequency offsets of each fat component are known *a priori*; therefore the unknown parameters are S_0 , $PDFF$, f_B and R_2^* . Note that this formulation slightly differs from that in²², where the parameters included ρ_f and ρ_w rather than S_0 and $PDFF$. The current formulation has been chosen as it allows a more convenient estimation of S_0 after the DL-based estimation of PDFF and R_2^* , as detailed in Section 3.1.4.

In the presence of Gaussian noise (present in both real and imaginary channels), the log likelihood for a set of predicted signals, given the measured signals, is given by

$$\log L(\{S_i\}, \sigma^2 | \{S'_i\}) = -n \log(\sqrt{2\pi\sigma^2}) - \sum_{i=1}^n \frac{|S'_i - S_i|^2}{2\sigma^2} \quad (2)$$

where $\{S_i\}$ is the set of predicted signals based on the parameter estimates, $\{S'_i\}$ is the set of measured signals, σ^2 is the variance of the Gaussian distribution for the noise, n is the number of measurements (double the number of echo times for complex data, or the number of echo times for magnitude data).

For the signal magnitude, the noise-free signal in Eqn (1) becomes

$$M(t|S_0, PDFF, R_2^*) = S_0 \left| (1 - PDFF) + PDFF \sum_{m=1}^M r_m e^{i2\pi f_{F,m} t} \right| e^{-tR_2^*} \quad (3)$$

with only three unknown parameters: S_0 , $PDFF$, and R_2^* .

Taking the magnitude dictates that the noise now has a Rician distribution. The log likelihood for a set of predicted signals becomes

$$\log L(\{M_i\}, \sigma^2 | \{M'_i\}) = \sum_{i=1}^n \left[\log \frac{M'_i}{\sigma^2} - \frac{M_i'^2 + M_i^2}{2\sigma^2} + \log I_0\left(\frac{M'_i M_i}{\sigma^2}\right) \right] \quad (4)$$

where $\{M'_i\}$ is the set of measured magnitude signals at different echo times, $\{M_i\}$ is the corresponding set of predicted magnitude signals and I_0 is the 0th order modified Bessel function of the first kind.

2.2 | Dual optima problem and the source of degeneracy in CSE-MRI

With magnitude-based fitting, the likelihood functions defined in Eqns (2) and (4) have two optima: one ‘true’ solution corresponding closely to the ground truth and one incorrect ‘swapped’ solution with a PDFF value at the opposite end of the range (i.e. with a PDFF value close to 1 - PDFF) (Fig. 1). This creates a source of degeneracy - for a given set of signals, there are two candidate solutions which have very similar likelihood. The MAGO and MAGORINO methods used two-point search to ensure that both optima are explored^{21,22}, and thus ensure that the global optimum would correspond to the true solution. However, this degeneracy can create a problem for deep learning, as outlined in Section 2.4.

Note that there is a stationary or ‘switching’ point close to 60% in the PDFF dimension, below which the initial guesses are likely to converge to the low PDFF solution and above which the initial guesses are likely to converge to the high PDFF solution (in 2D this is a saddle or minimax point) - this

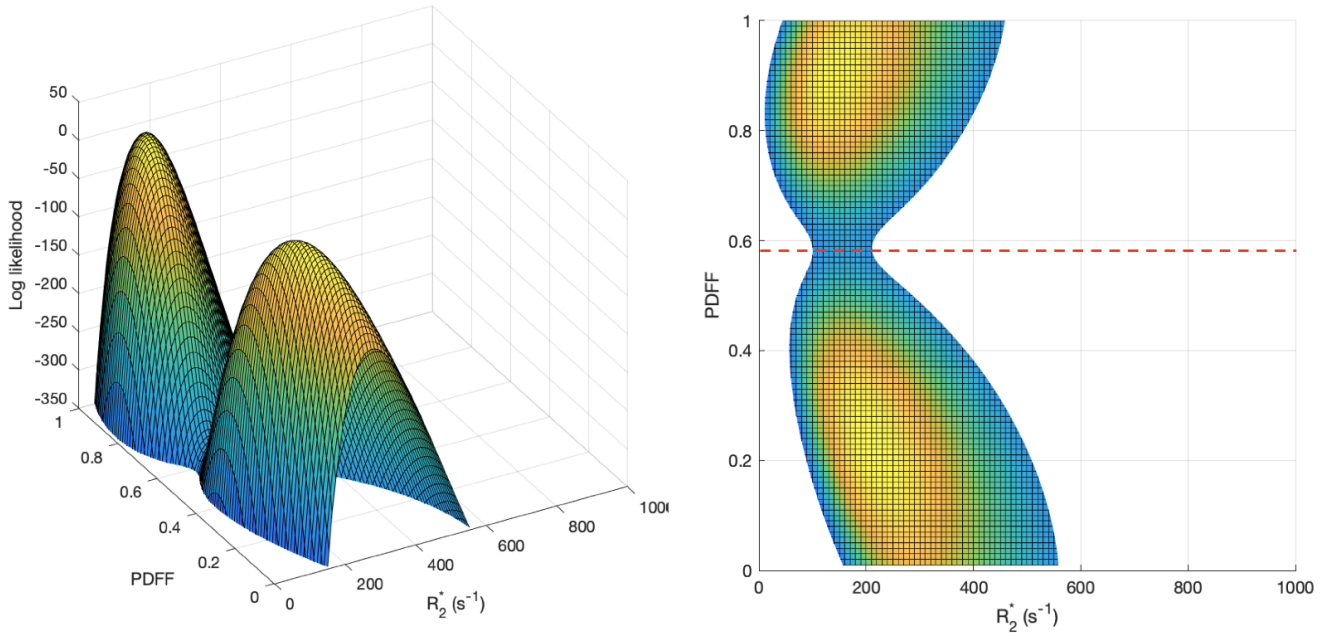


FIGURE 1 Illustration of dual-optimum problem. The Rician log likelihood is shown as a function of PDFF and R_2^* for a voxel with PDFF = 0.2 and $R_2^* = 200 \text{ s}^{-1}$ (oblique view, left, and top-down view, right). There are two optima, occurring at low PDFF (in this case this corresponds to the true solution) and high PDFF (in this case this corresponds to the swapped solution). This creates a source of degeneracy - for a given set of signals, there are two candidate solutions which have very similar likelihood, creating a ‘one-to-many’ problem which traditionally deep learning approaches are poorly equipped to solve. The switching line at PDFF = 0.58 (explained in Section 3.2.2) is shown as a dotted red line.

switching point is shown in Figure 1. This is relevant to the degeneracy problem discussed in Section 2.4.

2.3 | Parameter estimation with deep learning

The use of deep learning for curve fitting was first proposed by Bishop³⁵, and in recent years has become increasingly widely used for qMRI parameter estimation. As with conventional fitting, a model is fit to the acquired measurements. However, instead of finding the points on the objective function at which error is minimized / likelihood is maximised, a deep neural network is trained to directly map a single voxel’s signal to its corresponding qMRI parameters³⁵. The unknowns in this model are thus the network weights rather than the parameters in the signal model. Once the network has been trained, parameter estimation can be achieved by inputting unseen data to the network; the parameter estimates are then calculated in a single shot. This effectively front-loads the computational cost and means that the cost at the time the network is applied is dramatically reduced compared to conventional fitting.

2.4 | Degeneracy in deep learning

Bishop noted that neural networks were able to represent one-to-one and many-to-one mappings, but could not represent one-to-many (‘multivalued’) mappings³⁵. This problem was

referred to by Bishop as an ‘ambiguity phenomenon’ and is referred to here as degeneracy. In Bishop’s experiments, the quality of the neural network fits was found to be very poor in regions of parameter space where this degeneracy problem occurred. Guerreri et al. recently provided further theoretical insights into this problem, showing that, in the presence of degenerate samples during supervised training, the function learned by the neural network will map the degenerate signal to the empirical mean of tissue properties over the degenerate subset³⁶. In other words, in this situation the network does not learn either of the correct solutions.

This creates a problem for CSE-MRI, where a one-to-many problem of this type exists because there are two sets of parameter values (the ‘true’ solution and the ‘swapped’ solution) which correspond to very similar signals. Bishop suggested that, in cases where there were multiple potential solutions for a given input, this problem could be solved by excluding a region of the output space³⁵. However, this approach assumes that one region of output space can be discarded on the basis that it is unlikely to occur in experiment. With CSE-MRI, this is not a satisfactory solution because both low PDFF and high PDFF values can be present in real tissue.

To address this, we propose dividing the parameter space into two parts, in such a way that one network can be trained on the first part of parameter space, and the other network

can be trained on the second part of parameter space, without degeneracy. Specifically, we divide the parameter space into low PDFF regions, with PDFF values below the switching line, and high PDFF regions, with PDFF values above the switching line. The value of the switching line is chosen by inspecting the objective functions shown in Figure 1 to determine the location of the switching point in the PDFF dimension^{21,22}; further implementation details are provided in Section 3.2.2.

By dividing the training distribution in this way and training separate networks, we create two networks that are each accurate within the region of parameter space on which they are trained. We propose that the correct output of the two networks can then be chosen based on the difference in likelihood (as defined in Eqn (4)) between the two solutions.

3 | METHODS

3.1 | Network

An overview of the training procedures for single and dual network approaches and the inference procedure for the dual network approach is provided schematically in Figure 2 ; detail on, and justification of, the individual elements within this schematic is provided in the following subsections.

3.1.1 | Normalization using single peak approximation of S_0

To make network predictions robust to variations in signal intensity (i.e. variations in S_0), the multi-echo signals were normalized by a rough approximation of S_0 before being inputted to the network(s); this step was applied both during training and at inference (see Figure 2). Note that this step is not expected to produce accurate parameter estimates, and it is anticipated that the network learns to compensate for inaccuracies in this step.

This rough S_0 approximation, denoted \hat{S}_0 , was obtained by taking the measured signal for the two echo times closest to the first and second ‘in-phase’ echo times (assuming a single peak model), calculating the decay between these echo times (assuming monoexponential decay) and then extrapolating back to $t = 0$. To ensure that this did not result in an \hat{S}_0 lower than the maximum measured signal intensity, if $\hat{S}_0 < \max M(t)$, then \hat{S}_0 was set to be equal to $\max M(t)$.

For simulation experiments, this normalization step is not strictly necessary because S_0 is specified and therefore known *a priori*, however, we included this step in these experiments (as well as for the real data) to ensure that the results were as fair a representation as possible of the situation expected *in vivo*, where S_0 is unknown.

3.1.2 | Network architecture

We used a simple network design consisting of six layers in total - five fully-connected hidden layers, each with the same number of nodes as the number of signal measurements (i.e. echo times), and an output layer with a node for each model parameter (i.e. one output node for PDFF and one for R_2^*), with exponential linear unit (ELU) activation functions^{37,29}. This design is similar to Barbieri et al. and Epstein et al.^{28,29}, but uses five layers rather than three to increase network capacity; this was found to produce a small benefit in performance (further increases in network depth and width were tested but produced little benefit, and came with increased training time). The network was implemented in Matlab 2021b on an Apple iMac with 3.8-GHz 8-Core Intel i7 processor using the central processing unit (CPU).

3.1.3 | Network training

The network was trained in a supervised fashion using parameter values (labels) randomly drawn from PDFF / R_2^* parameter space (using a uniform distribution within the defined parameter ranges to minimise bias³⁰) and the corresponding simulated signal intensities (features). Noise was added to the training data with SNR values randomly sampled from a uniform distribution between 20 (very low SNR) and 120 (very high SNR, designed to exceed the upper end of the SNR range expected *in vivo*^{21,22}). Training was performed using an Adam optimiser with learning rate 0.001²⁹, mini-batch size 32, validation patience 50 (more conservative than Barbieri et al.²⁸, who used validation patience of 10). L2 regularisation was not used. Each network was trained using 100,000 samples²⁹, split 80/20 between training and validation. All processing was performed in MATLAB 2021b (MathWorks, Natick, MA). Further details of network training are detailed in the individual experiments below. Network training took approximately 90 minutes for the two network approach shown in Figure 2 .

3.1.4 | Network output selection based on likelihood

To determine which of the two networks’ predictions should be taken as the final output, the likelihood for the predicted signals from each network, given the measured signals, was compared.

To enable this, we first reformulate Eqn (3) as

$$M(t|S_0, PDFF, R_2^*) = S_0 a_t \quad (5)$$

where a_t is a known real-valued scalar quantity, calculated from the RAIDER parameter estimates using

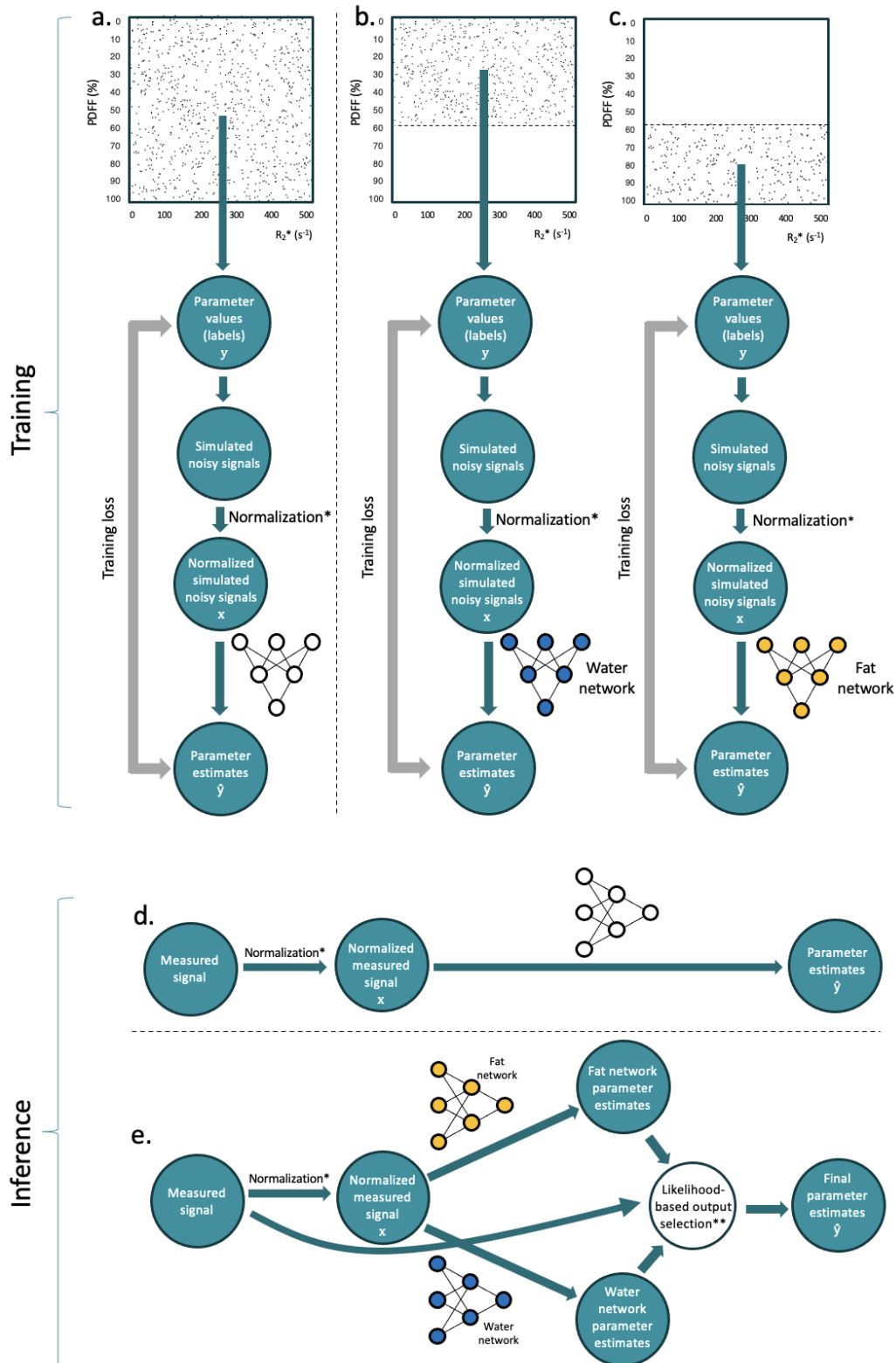


FIGURE 2 Training procedure for single (a) and dual (b,c) network approaches, and inference procedure for single network (d) and dual network (e) approaches. With a naive single network approach (a), one network is trained with a uniform distribution across the entire space of plausible parameter values. With the proposed approach, two separate networks are trained on separate parts of the plausible parameter space to avoid degeneracy: a ‘water network’ (b) is trained only on the region of parameter space below the ‘switching line’ (dashed line), and a ‘fat network’ (c) is trained only on the region of parameter space above the switching line (dashed line). At inference, for the dual network approach (e), the outputs from the two networks (fat network and water network) are treated as ‘candidate’ solutions; the likelihood for each candidate is calculated based on the measured signal and the one with the higher likelihood is selected (e). *Normalization is performed as detailed in 3.1.1. **The selection of either the water network or fat network output is performed as described in 3.1.4.

$$a_t = |(1 - PDFF) + PDFF \sum_{m=1}^M r_m e^{i2\pi f_{F,m} t}| e^{-tR_2^*}. \quad (6)$$

Once noise has been added, a new estimate of S_0 , \tilde{S}_0 , (note that this is distinct from the earlier, rough approximation \hat{S}_0) at the maximum Gaussian likelihood can be obtained using the matrix formulation

$$M = A\tilde{S}_0 \quad (7)$$

where M is a $N \times 1$ vector of measured signal magnitudes and A is a $N \times 1$ vector containing the values of a_t for each echotime, and N is the total number of echotimes. \tilde{S}_0 can be estimated using

$$\tilde{S}_0 = (A^T A)^{-1} A^T M \quad (8)$$

Having calculated S_0 , the log likelihood for the predicted signals, based on the measured signals, was calculated using Eqn (4) for each of the two networks' parameter estimates, and the network predictions giving the higher likelihood were taken as the output.

To facilitate selection of the correct network output in the occasional situation that one network produced high likelihood but physically implausible parameter estimates (specifically negative R_2^* values, which could occur when a network was exposed to signals outside its training distribution), such negative R_2^* values were deemed to be incorrect, and the outputs of the other network were selected.

3.2 | Simulation Experiments

A series of simulation experiments were conducted to investigate the effect of training data distribution on the accuracy and precision of parameter estimation.

For all of the experiments, the training data was constructed by simulating noise-free multi-echo signals using Eqn (3) for a range of PDFF and R_2^* values, using a typical CSE-MRI acquisition protocol with six echoes: $TE_1 = 1.152$ ms and $\Delta TE = 1.168$ ms, matching the first 3T protocol in Hernando et al.²⁶. The distribution of PDFF and R_2^* values was varied for each experiment by defining regions of parameter space from which the PDFF and R_2^* values could be selected, as detailed below and in Figure 2. PDFF and R_2^* values were randomly selected within the defined region.

Performance was evaluated on a separate simulated test dataset consisting of evenly-spaced PDFF and R_2^* values across the full parameter space ($PDFF \in [0, 1]$, $R_2^* \in [0, 500]$ s⁻¹), with 100 noisy signals (at SNR = 60, which is typical for CSE-MRI) for each PDFF / R_2^* combination. This resulted in $101 \times 21 \times 100 = 212100$ signal instantiations in total across all parameter values. Performance was evaluated in terms of the bias and precision of parameter estimates, and compared against conventional fitting with the MAGORINO

algorithm²², and also with an in-house implementation of the MAGO algorithm²¹.

3.2.1 | Single network with uniform training distribution

The training dataset consisted of 100,000 sets of magnitude signals derived from randomly-generated parameter combinations with a uniform distribution in PDFF / R_2^* parameter space ($PDFF \in [0, 1]$, $R_2^* \in [0, 500]$ s⁻¹), as demonstrated in Figure 2 (a).

3.2.2 | Dual networks with modified training distribution

To address the effect of degeneracy on network predictions, two training datasets, each consisting of 100,000 noise-free signal sets, were constructed from the following parameter distributions (as demonstrated in Figure 2 (b,c)):

The first network ('water network') was trained only on the low PDFF dataset, i.e. with PDFF values below the switching line ($PDFF \in [0, 0.58]$, $R_2^* \in [0, 500]$ s⁻¹).

The second network ('fat network') was trained only on the high PDFF dataset, i.e. with PDFF values above the switching line ($PDFF \in [0.58, 1]$, $R_2^* \in [0, 500]$ s⁻¹).

Having trained these two networks and obtained the predictions on the test dataset, a further set of 'composite' predictions was derived by choosing the output from the two networks with the highest likelihood, as described in Section 3.1.4.

3.3 | Phantom experiments

To evaluate the feasibility of DL-based fitting across a range of scanners, our method was evaluated in a publicly available multisite, multivendor, and multi-field-strength phantom data set²⁶. Full details of the dataset are given by Hernando et al.²⁶. Briefly, the dataset consists of fat-water mixtures with known varying fat fraction, scanned at 1.5 T and 3 T at six centers (two centers each for GE, Philips, and Siemens). Data acquisition was performed using each site's version of a multi-echo 3D spoiled gradient echo CSE sequence (six echo times), with two different protocols (each performed at 1.5T and 3T) performed in order to test the reproducibility across different acquisition parameters. Protocols 1 and 2 were performed at 1.5 T, and protocols 3 and 4 were performed at 3 T. Protocols 1 and 3 generated approximately in-phase and opposed-phased echoes, whereas protocols 2 and 4 used the shortest echoes achievable.

Deep learning-based parameter estimation was performed as described in Section 3.2.2. After generating parameter

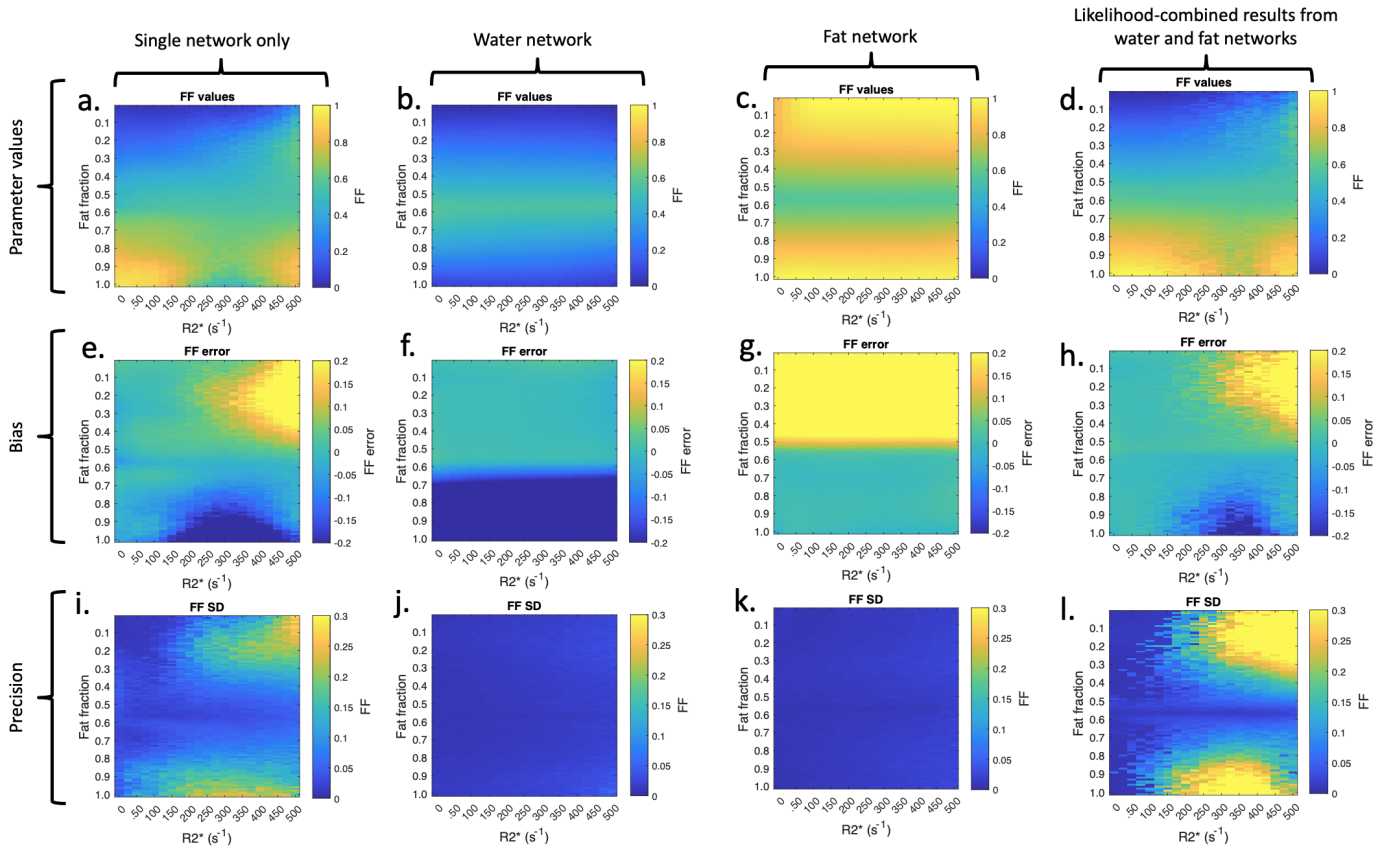


FIGURE 3 Improvement in performance for dual network approach compared to single network (evaluation in the presence of noise). The figure shows the performance of a single network with no restriction of training distribution (left column), individual water and fat networks (second and third columns) and likelihood-combined networks (right column). The parameter values are shown on the top row, bias is displayed in the middle row and parameter standard deviation is shown on the bottom row.

maps, fat fraction values were obtained from the individual vials of the phantom by taking the median value from ROIs placed on the individual tubes^{21,22} and compared against known reference values. The performance of the networks was compared against conventional fitting.

3.4 | In vivo imaging

To evaluate the feasibility of the proposed approach *in vivo*, we imaged the pelvis, lower legs and thorax/abdomen of three separate subjects. The pelvis and lower leg data were acquired on a 3T Philips Ingenia system using a multi-echo 3D spoiled gradient echo sequence with flyback gradients and monopolar readouts $TE_1 = 1.2$ ms, $\Delta TE = 1.6$ ms, six echoes, flip angle = 5° , $TR = 25$ ms, matrix size = 320×320 , and pixel spacing = 1.8×1.8 mm. The thoraco-abdominal imaging was performed on a Siemens 3T Vida scanner using a similar acquisition with $TE_1 = 1.1$ ms, $\Delta TE = 1.1$ ms. Deep learning-based parameter estimation was performed as described in Section 3.2.2; conventional magnitude-based fitting was performed using

both Gaussian and Rician noise models, as described previously^{21,22}. These scans were performed with institutional review board approval (Queen Square Research Ethics Committee, London, REC 15/LO/1475), and subjects provided written informed consent.

4 | RESULTS

4.1 | Simulation experiments

4.1.1 | Single network with uniform training distribution

Figure 3 (left column) shows the performance of a single network trained with a uniform distribution of parameter values over the full parameter space, evaluated in the presence of noise. At low PDF, there are regions of positive error (shown in yellow) towards the right of subplot (e) (i.e. with increasing R_2^*). Similarly, at high PDF, there are regions of negative error with increasing R_2^* . The precision of parameter estimates (i) also deteriorates with increasing R_2^* .

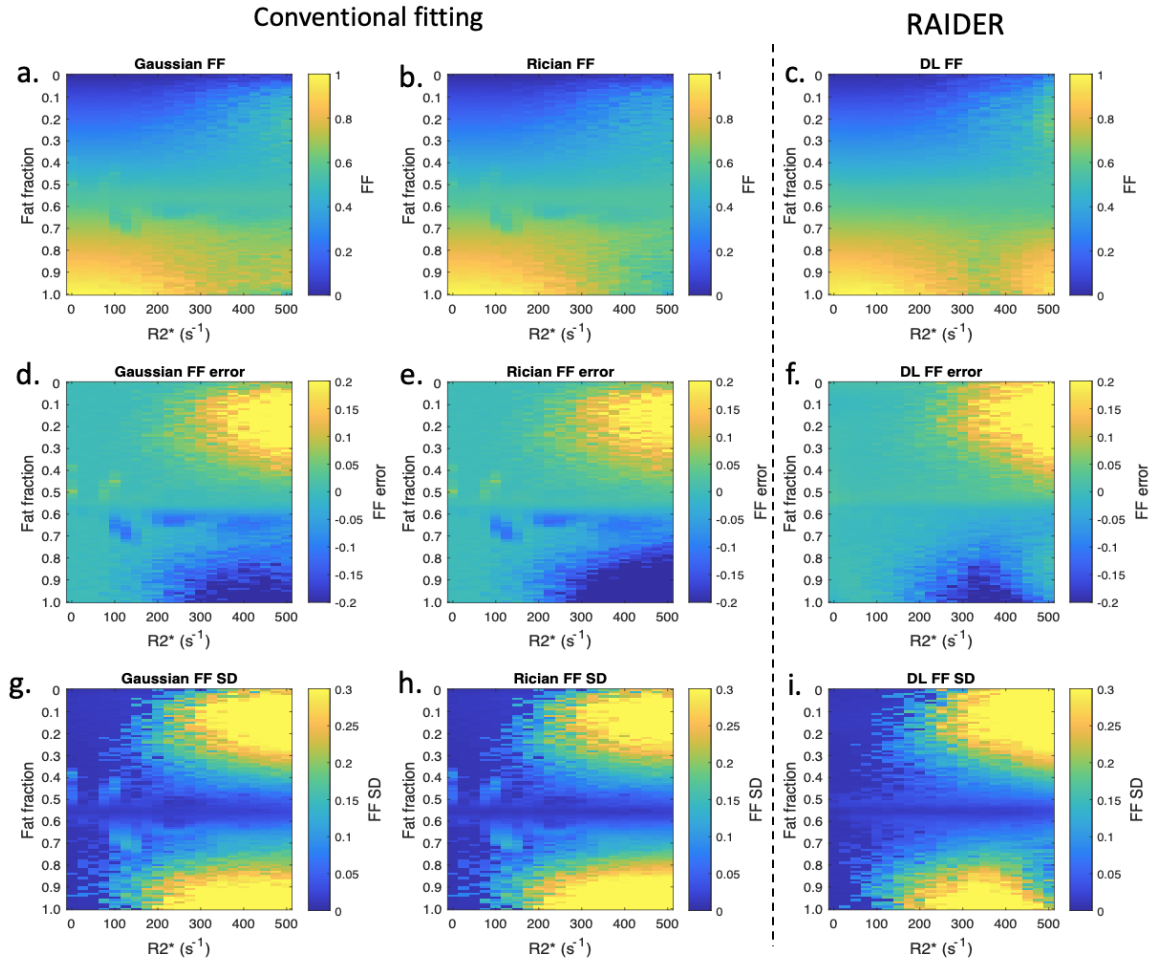


FIGURE 4 Performance of chosen PDFF output from two networks in the presence of noise and comparison against conventional fitting. The top row shows estimated parameter values, the middle row shows parameter bias, and the bottom row shows parameter variance. The left and middle columns refer to conventional fitting with Gaussian and Rician noise models, the right column refers to RAIDER.

For the full simulation experiment over 212100 signal instantiations, inference took 3.9s compared to 1649s (i.e. 27 minutes) for conventional fitting (423 fold acceleration).

4.1.2 | Dual networks with modified training distribution

The second column of Figure 3 shows the performance of a single network trained with a restricted, low PDFF distribution of parameter values (the ‘water network’), evaluated in the presence of noise. Compared to the single network, there is a substantial improvement in performance for low PDFF values, with elimination of the high error, high variance regions at high R_2^* . However, as expected, the network fails on the high PDFF values as it has not experienced this region of parameter space during training.

Similarly, the third column of Figure 3 shows the performance of a single network trained with a restricted, high PDFF distribution of parameter values (the ‘fat network’). Compared

to the single network, there is a substantial improvement in performance for high PDFF values, particularly at high R_2^* . As expected, the network fails on the low PDFF values as it has not experienced this region of parameter space during training.

The right-hand column of Figure 3 shows the ‘combined’ performance of the two networks (i.e. the performance of the chosen output of the two networks based on likelihood). Compared to the single network (left column), the performance is substantially improved, with a reduction in bias. Note that the increase in parameter standard deviation shown in the precision plot (l) compared to (i) reflects the fact that the parameter estimates are consistently biased towards the middle of the PDFF range in (i).

Figure 4 shows the combined performance of the two networks in terms of PDFF bias and precision, compared against conventional fitting in the presence of noise. The overall performance is slightly superior to conventional fitting using

Gaussian and Rician likelihood models. All three methods perform well at low PDFF.

Figure 5 shows the combined performance of the two networks in terms of R_2^* bias and precision, compared against conventional fitting in the presence of noise. Again, the overall performance is slightly superior to conventional fitting using Gaussian and Rician likelihood models.

For the full simulation experiment over 212100 signal instantiations, inference took 3.7s, again compared to 1649s (i.e. 27 minutes) for conventional fitting (446 fold acceleration).

4.2 | Phantom experiments

Results of the analysis of the multisite phantom data set are shown in Figure 6 .

Median PDFF values for all 11 phantom vials are plotted against reference fat fraction values for all sites, acquisition protocols, and field strengths. There is good agreement between the predictions and the reference values with minimal bias across vendors and field strengths, and the overall performance was similar for the two methods. Some small differences were observed: in particular, for protocol 2 RAIDER performed better at some sites in the pure fat (high FF) vial.

Inference for the entire set of 28 phantom datasets (one slice for each) took 47.5s (i.e. 1.7s per dataset) for RAIDER, compared to 5.1 hours (i.e. 11 minutes per dataset) for MAGORINO (385-fold acceleration).

4.3 | In vivo imaging

Images from the three subjects are shown in Figures 7 , 8 and 9 . Figure 7 illustrates how the outputs from the water network (a,e) and the fat network (b,f) are combined to produce the composite predictions shown in the third column (c,g). Figures 8 and 9 also include difference maps to demonstrate differences between methods in the various tissues. In all subjects, the composite predictions produced satisfactory fat–water separation across the image and good-quality R_2^* maps. Figure 7 shows good agreement between the composite predictions and conventional fitting. Figure 8 shows good agreement between RAIDER and conventional fitting, with slightly superior performance in the muscle for RAIDER but slightly inferior performance in the subcutaneous fat. Figure 9 shows close agreement between RAIDER and conventional fitting across a range of organs, including liver, kidneys and bone marrow.

Inference for the image slices shown in Figures 7 , 8 and 9 took 2.3s, 1.7s and 1.4s respectively, compared to 56 minutes, 8 minutes and 17 minutes for conventional fitting (1450-fold, 285-fold and 712-fold acceleration respectively). Note that the lower conventional fitting times for the second

dataset were because the background voxels with zero signal intensity at all echo times were recognised by MAGORINO as not needing fitting, meaning that the number of fitted voxels was substantially reduced.

5 | DISCUSSION

Recently, several groups have explored the use of magnitude-based fitting for estimating proton density fat fraction (PDFF) and R_2^* estimation from chemical shift-encoded MRI data, since this approach can be used when complex-based methods fail or when phase data are inaccessible or unreliable, such as in multi-centre studies or in low resource settings, and may also be used as a final processing step with complex-based methods. However, these methods are currently limited by their computational cost, increasing reconstruction time and financial cost and creating a barrier to their use. Unfortunately, convolutional neural networks (CNNs)^{31,32,33,34} are poorly placed to resolve these issues due to intrinsic limitations in terms of training data requirements and generalizability across anatomies, scanners and imaging protocols. Here, we propose RAIDER, which uses deep learning to separate water and fat in a ‘voxel-independent fashion’, performing parameter estimation separately in each voxel. The proposed method is trained in simulation and thus avoids the key limitations of CNN-based methods and also offers a substantial reduction in computational cost compared to conventional fitting.

The proposed RAIDER approach, using two networks, is motivated by our demonstration that using a single network with a full training distribution, including all plausible PDFF and R_2^* values, produces relatively poor performance, with substantial imprecision in PDFF estimates. Furthermore, the observation that parameter estimates are biased towards the mean is a strong indication that this problem is due to degeneracy³⁶. Crucially, we showed that performance could be substantially improved by training individual networks on a restricted distribution of parameter values: specifically, by training one network only on low PDFF values (below the switching line) and another on high PDFF values (above the switching line). By selecting the most likely result from these networks, we were able to obtain predictions that substantially outperformed a naive single network implementation across the full parameter space. This dual network deep learning-based method offered similar performance to conventional fitting in terms of bias and precision but was markedly faster, with a 285-1450-fold acceleration. We also showed that this method could be successfully implemented in multisite, multivendor phantom data and *in vivo*. Our results suggest that the proposed method could help to reduce the time and expense associated with processing of CSE-MRI data for research and in clinical practice.

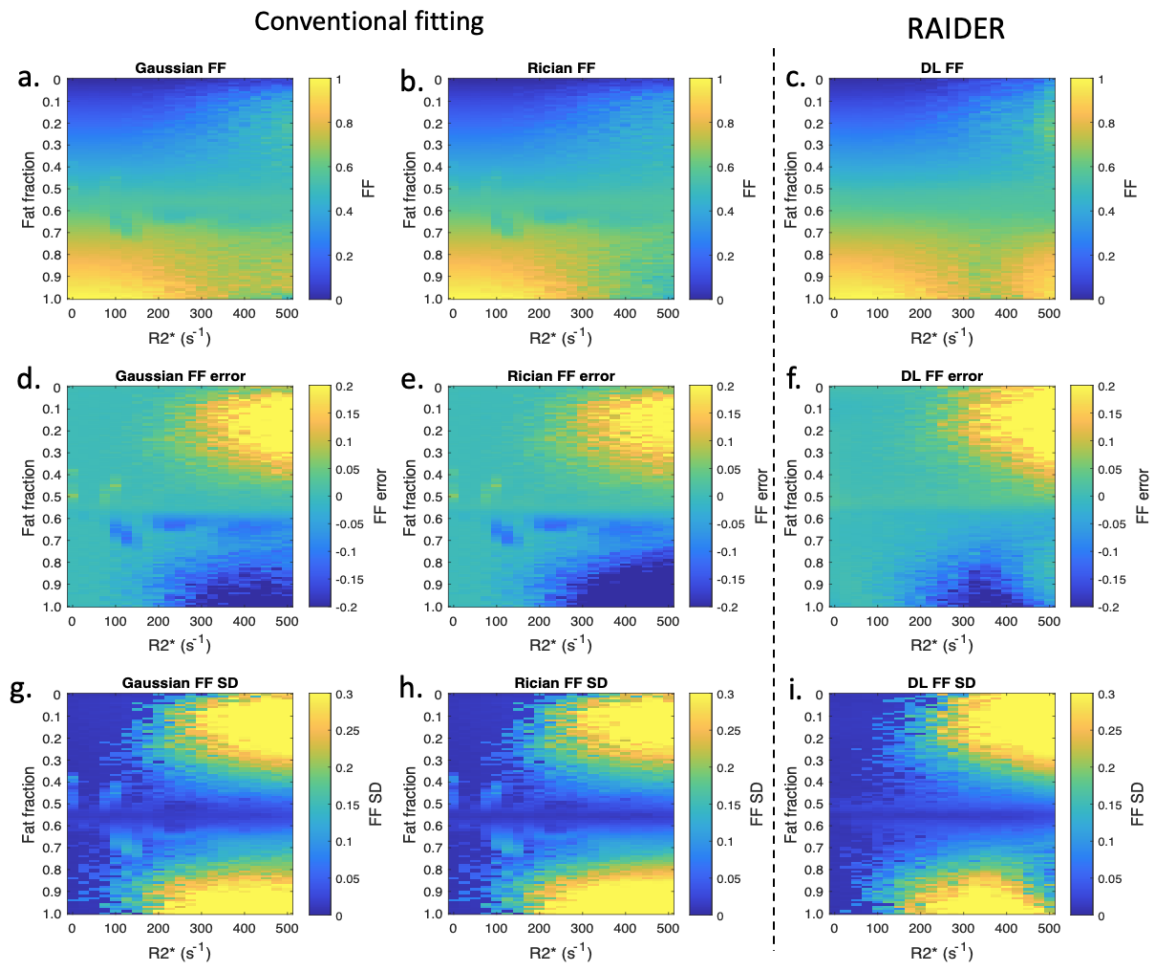


FIGURE 5 Performance of chosen R_2^* output from two networks in the presence of noise and comparison against conventional fitting. The top row shows estimated parameter values, the middle row shows parameter bias, and the bottom row shows parameter variance. The left and middle columns refer to conventional fitting with Gaussian and Rician noise models, the right column refers to RAIDER.

Notably, there is a parallel between the approach used in this work, where two networks are used to separately obtain low PDFF and high PDFF solutions, with the conventional fitting-based MAGO and MAGORINO methods, where fitting is initiated twice from two different start points in order to ensure that the global optimum on the likelihood function is found^{21,22}. Furthermore, the use of magnitude data retains the benefit of being essentially insensitive to B_0 inhomogeneity, meaning that it could help to reduce artefacts at the edges of the field and in challenging situations such as when near metal, when imaging large subjects or when imaging anatomically complex structures, such as the small bowel.

In principle it would also be straightforward to use the RAIDER networks to refine predictions of other methods within a multistep process, as is commonly done with conventional magnitude fitting^{27,26}, since the appropriate network (fat or water) could be chosen depending on the output of the previous step. Alternatively, RAIDER could be used as a

first processing step in the estimation of B_0 in the context of QSM¹⁸.

This work has some limitations. Firstly, under optimal conditions where the phase is completely reliable, the performance of magnitude-based methods, including the proposed RAIDER method as well as the existing MAGO and MAGORINO methods, may be inferior to complex-based methods as well as more sensitive to model mismatch^{38,39}. However, this class of methods is explicitly designed for situations where the phase is unavailable or unreliable, and can also be used to refine initial estimates produced by complex signal-based methods. As described in the Introduction, such magnitude-based approaches are increasingly seen as a practical and generalizable method. Additionally, the proposed RAIDER approach suggests a general approach to deep learning-based parameter estimation from multi-echo CSE-MRI data, and could also be adapted for complex fitting, where the degeneracy problem also exists. Further work is required to investigate the relative strengths and weaknesses

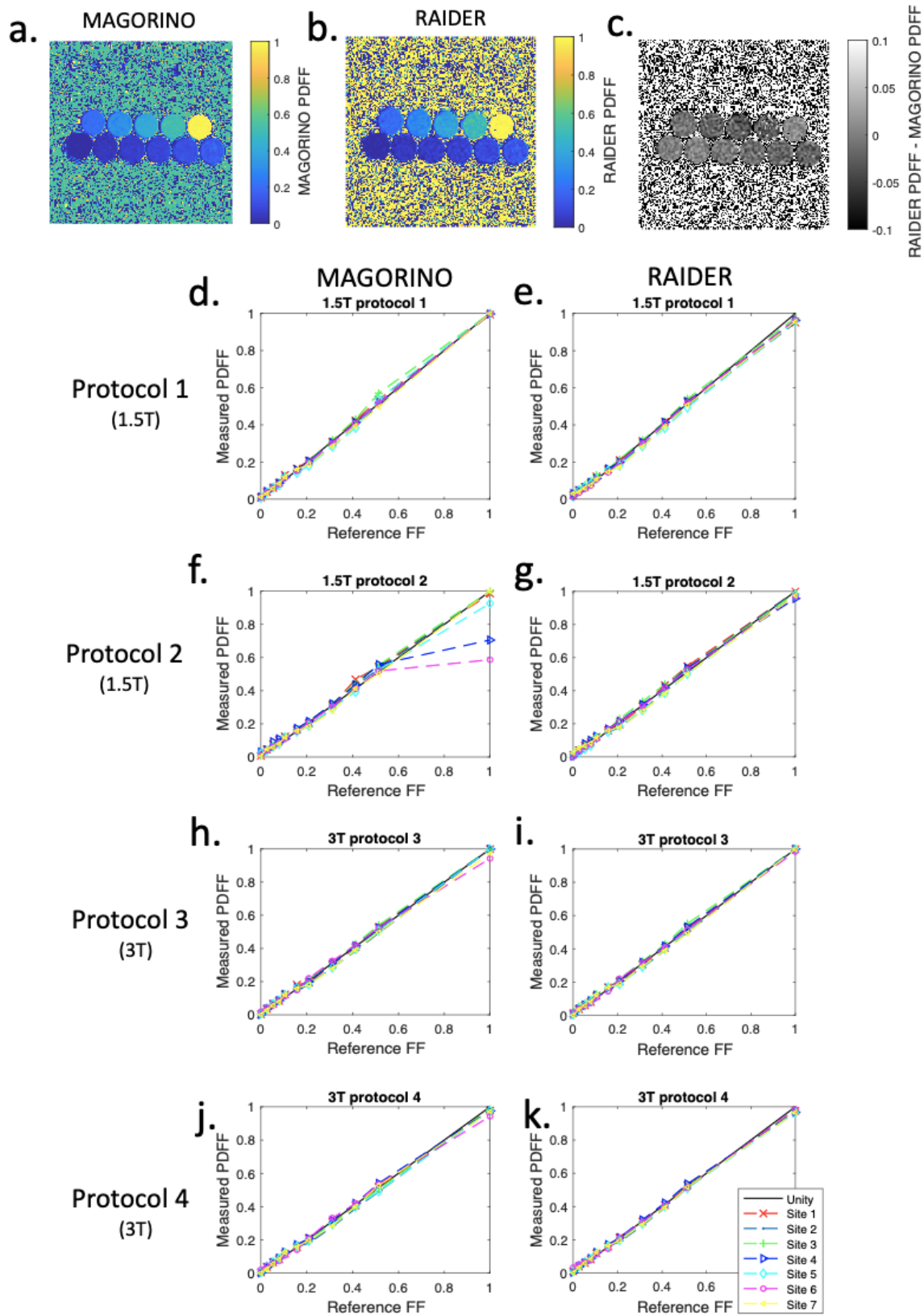


FIGURE 6 Results from multisite, multivendor, multi-field-strength phantom data set. Results from conventional fitting (MAGORINO) are shown in the left column, and RAIDER results are shown in the right column. Agreement plots are shown for each of the four protocols, with individual points for each of the six sites. The black line indicates perfect agreement with reference PDFF values. “Site 7” refers to the repeat scans at site 1. The example image (top) is from site 1, 3T protocol 2, chosen to enable a direct visual comparison with corresponding illustrations in the MAGO and MAGORINO papers^{21,22}. Reference FF values in the phantom were 0.026, 0.053, 0.079, 0.105, 0.157, 0.209, 0.312, 0.413, 0.514 and 1.

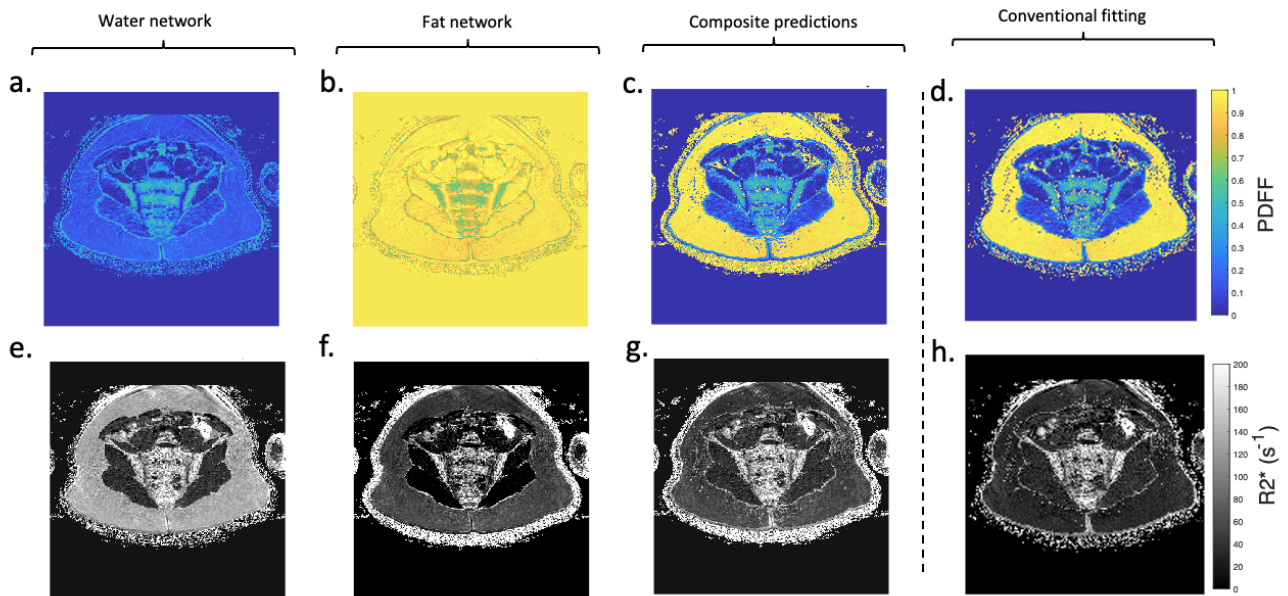


FIGURE 7 PDFF maps (top row) and R_2^* maps (bottom row) from the pelvis of a volunteer. Note that the water network (first column) produces exclusively low PDFF estimates whereas the fat network (second column) produces exclusively high PDFF estimates. However, the chosen output from the two networks based on likelihood (third column) produces plausible predictions across a range of tissue types, including adipose tissue (almost pure fat), muscle (almost pure water) and bone marrow (approximately equal fat and water content). These agree closely with conventional fitting (fourth column).

of different deep learning-based methods, and to consider how hybrid approaches (for example, combining deep learning and conventional fitting methods) might be used to balance speed and performance. Overall, the potential acceleration offered by deep learning-based methods offers to substantially accelerate and simplify PDFF and R_2^* estimation. Secondly, this is a ‘proof-of-concept’ study, describing a new methodological approach, and the evaluation with real data is preliminary. Thirdly, in its present form the method does not account for Rician noise in its training procedure (although this is considered at the output selection step), which may create bias at low SNR, for example in tissues with low proton density, very high R_2^* or at low field strength. This could be addressed by incorporating alternative DL approaches such as self-supervised learning^{29,28} into the current framework. Similarly, the method may perform less well in atypical tissues which produce signals that deviate further from those encountered in the training dataset, such as in cortical bone where the SNR is very low. However, for most existing clinical applications this is of little concern, and the training method could potentially be modified for the tissues in question if needed. Fourthly, the current implementation produced slightly biased R_2^* estimates in subcutaneous fat, likely because the single peak normalization procedure (see 3.1.1) is imperfect and can result in more inaccurate S_0 estimates in this tissue due to fat-fat interference; this issue may be addressed by developing improved normalization strategies.

6 | CONCLUSIONS

The paired neural network approach employed by RAIDER resolves the problems posed by degeneracy, avoids the training limitations of CNN-based methods and substantially reduces computational cost compared to conventional fitting.

DATA AVAILABILITY

The code for RAIDER implementation is available at <https://github.com/TJPBray/DixonDL>. The code used to generate the results in this paper are preserved in their original form as release v1.0 in the Dixon DL repository.

Financial disclosure

TJPB and MHC were supported by the UCLH National Institute for Health Research Biomedical Research Centre. This work was undertaken at UCLH/UCL, which receives funding from the UK Department of Health’s NIHR BRC funding scheme. The funders had no role in study design, data collection and analysis, decision to publish, or preparation of the manuscript.

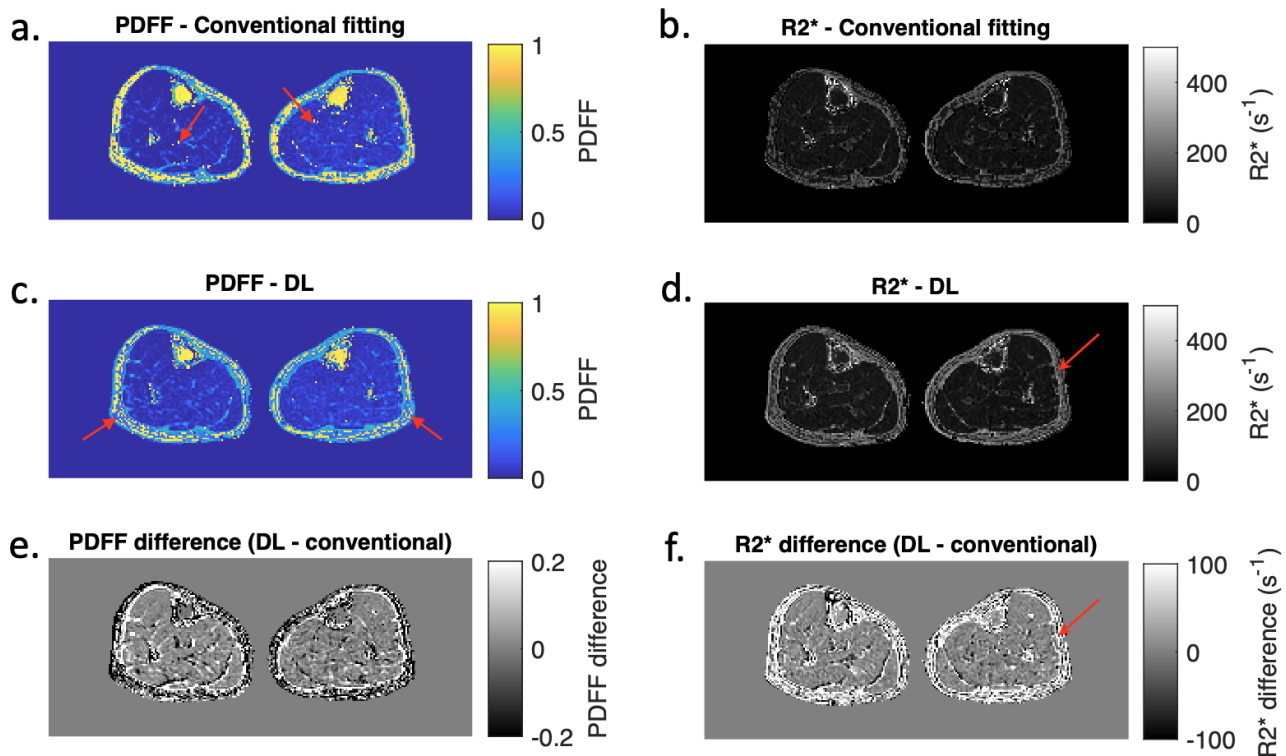


FIGURE 8 Images of the lower legs in a volunteer. PDFF maps (left column) and R_2^* maps (right column) are shown: the top row contains maps produced with conventional fitting, the middle row shows the deep learning-produced maps, and the bottom row shows difference maps. The DL-based maps show fewer swapped voxels in the muscle (these swapped voxels are arrowed in a), but in this dataset shows a slightly higher proportion of swapped voxels in the subcutaneous fat (arrowed in b). The deep learning method also produced slightly positively biased R_2^* estimates in subcutaneous fat (d,f). Note that very low signal voxels in the background were masked out and are seen as 0s to increase the clarity of the Figure.

Conflict of interest

The authors declare no potential conflict of interests.

ORCID

Timothy JP Bray [ORCID](#) 0000-0001-8886-5356

Giulio V Minore [ORCID](#) 0009-0001-4529-8547

Alan Bainbridge [ORCID](#) 0000-0003-4941-5840

Louis Dwyer-Hemmings

Stuart A Taylor [ORCID](#) 0000-0002-6765-8806

Margaret A Hall-Craggs [ORCID](#) 0000-0003-4941-5840

Hui Zhang [ORCID](#) 0000-0002-5426-2140

REFERENCES

1. SB Reeder, Z Wen, H Yu, AR Pineda, GE Gold, M Markl, and NJ Pelc. Multicoil Dixon chemical species separation with an iterative least-squares estimation method. *Magn Reson Med*, 51(1): 35–45, 2004.
2. SB Reeder, AR Pineda, Z Wen, A Shimakawa, H Yu, JH Brittain, GE Gold, CH Beaulieu, and NJ Pelc. Iterative decomposition of water and fat with echo asymmetry and least-squares estimation (IDEAL): Application with fast spin-echo imaging. *Magn Reson Med*, 54(3):636–644, 2005.
3. D Hernando, JP Haldar, J Ma, P Kellman, and Z-P Liang. Joint estimation of water/fat images and field inhomogeneity map. *Magn Reson Med*, 59(3):571–80, 2008.
4. CY Liu, CA McKenzie, H Yu, JH Brittain, and SB Reeder. Fat quantification with IDEAL gradient echo imaging: Correction of bias from T1 and noise. *Magn Reson Med*, 58(2):354–64, 2007.
5. M Nouredin, J Lam, MR Petereson, M Middleton, G Hamilton, T-A Le, R Betterncourt, C Changchien, DA Brenner, C Sirlin, and R Loomba. Utility of magnetic resonance imaging versus histology for quantifying changes in liver fat in nonalcoholic fatty liver disease trials. *Magn Reson Med*, 58(6):1930–1940, 2013.
6. TJP Bray, MD Chouhan, S Punwani, A Bainbridge, and MA Hall-Craggs. Fat fraction mapping using magnetic resonance imaging: insight into pathophysiology. *Br J Radiol*, 91:1089, 2018.
7. JH Yoon, JM Lee, KB Lee, SW Kim, MJ Kang, JY Jang, S Kanngiesser, JK Han, and BI Choi. Pancreatic steatosis and fibrosis: quantitative assessment with preoperative multiparametric MR imaging. *Radiology*, 279:140–150, 2016.
8. JP Kuhn, F Berthold, J Mayerle, H Volzke, SB Reeder, W Rathman, MM Lerch, N Hosten, K Hegenscheid, and PJ Meffert. Pancreatic steatosis demonstrated at MR imaging in the general population: clinical relevance. *Radiology*, 276(1):129–136, 2015.

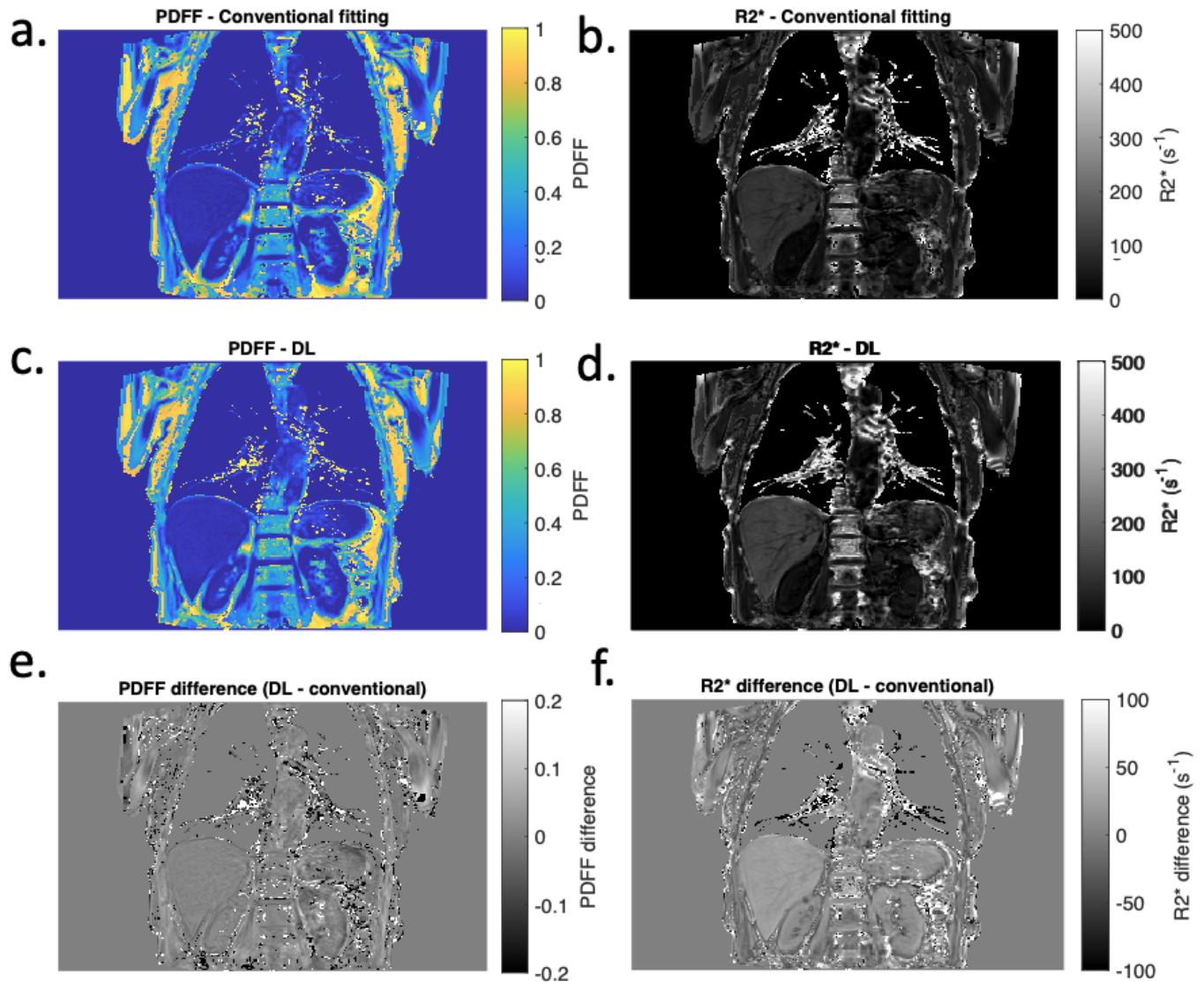


FIGURE 9 Images of the thorax and abdomen in a volunteer. PDFF maps (a,c) and R_2^* maps (b,d) as well as difference maps (e,f) are shown: the top row contains maps produced with deep learning, the middle row shows the vendor-generated maps. There are minimal differences in PDFF and R_2^* between methods across a range of tissues including liver, kidney and bone marrow. A small positive R_2^* bias is noted in the liver and kidneys. Note that very low signal voxels (in the background and lungs) were masked out to increase the clarity of the Figure and are seen as 0s.

9. JM Morrow, CDJ Sinclair, A Fischmann, P Machado, MM Reilly, TA Yousry, JS Thornton, and MG Hanna. MRI biomarker assessment of neuromuscular disease progression: a prospective observational cohort study. *Lancet Neurol*, 15(1):65–77, 2016.
10. TJP Bray, A Bainbridge, S Punwani, Y Ioannou, and MA Hall-Craggs. Simultaneous quantification of bone edema/adiposity and structure in inflamed bone using chemical shift-encoded MRI in spondyloarthritis. *Magn Reson Med*, 79(2):1031–1042, 2018.
11. A Latifoltojar, MA Hall-Craggs, A Bainbridge, N Rabin, R Popat, A Rismani, S D'Sa, N Dikaois, M Sokolsa, M Antonelli, S Ourselin, K Yong, SA Taylor, S Halligan, and S. Punwani. Whole-body MRI quantitative biomarkers are associated significantly with treatment response in patients with newly diagnosed symptomatic multiple myeloma following bortezomib induction. *Eur Radiol*, 27(12): 5325–5336, 2017.
12. SA Taylor, SM Mallett, S Ball, S Beare, G Bhatnagar, A Bhowmik, P Boavida, J. Bridgewater, et al. Diagnostic accuracy of whole-body MRI versus standard imaging pathways for metastatic disease in newly diagnosed non-small-cell lung cancer: the prospective Streamline L trial. *Lancet Resp*, 7(6):523–532, 2019.
13. SA Taylor, SM Mallett, S Beare, G Bhatnagar, D Blunt, P Boavida, J. Bridgewater, et al. Diagnostic accuracy of whole-body MRI versus standard imaging pathways for metastatic disease in newly diagnosed colorectal cancer: the prospective Streamline C trial. *Lancet Gastro Hep*, 4(7):529–537, 2019.
14. CM Costelloe, V Kundra, J Ma, BA Chasen, EM Rohren, RL Bassett, and JE Madewell. Fast Dixon whole-body MRI for detecting distant cancer metastasis: a preliminary clinical study. *J Magn Reson Imaging*, 35(2):399–408, 2012.

15. V Choida, A-V Madenidou, D Sen, MA Hall-Craggs, and C Ciurtin. The role of whole-body MRI in musculoskeletal inflammation detection and treatment response evaluation in inflammatory arthritis across age: A systematic review. *J Magn Reson Imaging*, 52: 151953, 2022.
16. T Kirchgessner, S Acid, V Perlepe, F Lecouvet, and B Vande Berg. Two-point Dixon fat-water swapping artifact: lesion mimicker at musculoskeletal T2-weighted MRI. *Skeletal Radiology*, 49:2081–2086, 2020.
17. N Bastay, M Thanaj, M Cule, EP Sorokin, Y Liu, EL Thomas, JD Bell, and BW Whitcher. Artifact-free fat-water separation in dixon MRI using deep learning. *J Big Data*, 10:4, 2023.
18. A Triay Bagur, D McClymont, C Hutton, A Borghetto, ML Gyngell, P Alijabar, MD Robson, M Brady, and DP Bulte. Estimation of field inhomogeneity map following magnitude-based ambiguity-resolved water-fat separation. *Magn Reson Imag*, 97:102–111, 2023.
19. I Khodarahmi, A Isaac, EK Fishman, D Dalili, and J Fritz. Metal about the hip and artifact reduction techniques: from basic concepts to advanced imaging. *Sem Musc Radiol*, 23(3):e68–81, 2019.
20. D Boone and SA Taylor. Magnetic resonance of the small bowel: how to do it. 2020.
21. A Triay Bagur, C Hutton, B Irving, ML Gyngell, MD Robson, and M Brady. Magnitude-intrinsic water–fat ambiguity can be resolved with multipeak fat modeling and a multipoint search method. *Magn Reson Med*, 82(1):460–475, 2018.
22. TJP Bray, A Bainbridge, MA Hall-Craggs, and H Zhang. MAGORINO: Magnitude-only fat fraction and R_2^* estimation with Rician noise modelling. *Magn Reson Med*, 89:1173–1192, 2022.
23. WJ Wong, C Emdin, AG Bick, SM Zekavat, A Niroula, JP Pirruccello, L Dichtel, G Griffin, MM Uddin, CJ Gibson, V Kovalcik, AE Lin, ME McConkey, A Vromman, RS Sellar, PG Kim, M Agrawal, J Weinstock, MT Long, B Yu, R Banerjee, RC Nicholls, A Dennis, M Kelly, PR Loh, S McCarroll, E Boerwinkle, RS Vasani, S Jaiswal, AD Johnson, RT Chung, K Corey, D Levy, C Ballantyne, BL Ebert, and Natarajan P. Clonal haematopoiesis and risk of chronic liver disease. *Nature*, 616:747–754, 2023.
24. T Waddell, A Bagur, D Cunha, H Thomaides-Brears, R Banerjee, DJ Cuthbertson, E Brown, K Cusi, JP Despres, and M Brady. Greater ectopic fat deposition and liver fibroinflammation and lower skeletal muscle mass in people with type 2 diabetes. *Obesity*, 30:1231–1238, 2022.
25. V Losev, C Lu, DS Senevirathne, P Inglese, W Bai, AP King, M Shah, A de Marvao, and DP O'Regan. Body fat and human cardiovascular ageing. *medRxiv*, 2024.
26. D Hernando, SD Sharma, MA Ghasabeh, BD Alvis, SS Arora, G Hamilton, L Pan, and JM Shaffer. Multisite, multivendor validation of the accuracy and reproducibility of proton-density fat-fraction quantification at 1.5T and 3T using a fat–water phantom. *Magn Reson Med*, 77:1516–1524, 2017.
27. X Zhong, MD Nickel, SA Kannengiesser, BM Dale, B Kiefer, and MR Bashir. Liver fat quantification using a multi-step adaptive fitting approach with multi-echo GRE imaging. *Magn Reson Med*, 72: 1353–1365, 2014.
28. S Barbieri, O Gurney-Champion, R Klaassen, and H Thoeney. Deep learning how to fit an intravoxel incoherent motion model to diffusion-weighted MRI. *Magn Reson Med*, page 27910, 2019.
29. S Epstein, TJP Bray, MA Hall-Craggs, and H Zhang. Choice of training label matters: how to best use deep learning for quantitative MRI parameter estimation. *J Mach Learn Biomed Imaging*, 2:586–610, 2024.
30. N Gyori, M Palombo, CA Clark, H Zhang, and DC Alexander. Training data distribution significantly impacts the estimation of tissue microstructure with machine learning. *Magn Reson Med*, page 29014, 2021.
31. JW Goldfarb, J Craft, and JJ Cao. Water–fat separation and parameter mapping in cardiac MRI via deep learning with a convolutional neural network. *J Magn Reson Imag*, 50:655–665, 2019.
32. J Andersson, H Ahlström, and J Kullberg. Separation of water and fat signal in whole-body gradient echo scans using convolutional neural networks. *Magn Reson Med*, 82:1177–1186, 2019.
33. R Jafari, P Spincemaille, J Zhang, TD Nguyen, X Luo, J Cho, D Margolis, MR Prince, and Y Wang. Deep neural network for water/fat separation: Supervised training, unsupervised training, and no training. *Magn Reson Med*, 85:2253–2277, 2021.
34. K Liu, Xiaojun Li, Y Chen, H Xiong, F Chen, Qinjia Bao, and C Liu. Robust water–fat separation based on deep learning model exploring multi-echo nature of mGRE. *Magn Reson Med*, 85:2828–2841, 2021.
35. CM Bishop and CM Roach. Fast curve fitting using neural networks. *Rev Sci Instrum*, 63(10):4450–4456, 1992.
36. M Guerreri, S Epstein, H Azadbakht, and H Zhang. Resolving quantitative MRI model degeneracy with machine learning via training data distribution design. *Inf Process Med Imaging*, 2023.
37. DA Clevert, T Unterthiner, and S Hochreiter. Fast and accurate deep network learning by exponential linear units (ELUs). *arXiv*, page 1511.07829, 2015.
38. D Hernando, Z-P Liang, and P Kellman. Chemical shift-based water/fat separation: A comparison of signal models. *Magn Reson Med*, 64:811–822, 2010.
39. X Wang, D Hernando, and SB Reeder. Sensitivity of chemical shift-encoded fat quantification to calibration of fat MR spectrum. *Magn Reson Med*, 75:845–851, 2016.

SUPPORTING INFORMATION

The following supporting information is available as part of the online article:

How to cite this article: TJP Bray, GV Minore, A Bainbridge, L Dwyer-Hemmings, SA Taylor, MA Hall-Craggs, and H Zhang (2024), RAIDER: Rapid, anatomy-independent, deep learning-based PDF and R_2^* estimation using magnitude-only signals, *Magn Reson Med*, 2024;00:1–6.